

## Analysis of an autonomous phase model for neuronal parabolic bursting

S. M. Baer<sup>1</sup>, J. Rinzel<sup>2</sup>, H. Carrillo<sup>3</sup>

<sup>1</sup> Department of Mathematics, Arizona State University, Tempe, AZ 85287-1804, USA

<sup>2</sup> Mathematical Research Branch, NIDDK, National Institutes of Health, Bethesda, MD 20892, USA

<sup>3</sup> Laboratorio de Dinamica No Lineal, Facultad de Ciencias, Universidad Nacional Autonoma de Mexico, Mexico 04510, D.F.

Received 3 September 1993; received in revised form 2 May 1994

**Abstract.** An understanding of the nonlinear dynamics of bursting is fundamental in unraveling structure-function relations in nerve and secretory tissue. Bursting is characterized by alternations between phases of rapid spiking and slowly varying potential. A simple phase model is developed to study endogenous parabolic bursting, a class of burst activity observed experimentally in excitable membrane. The phase model is motivated by Rinzel and Lee's dissection of a model for neuronal parabolic bursting (J. Math. Biol. 25, 653–675 (1987)). Rapid spiking is represented canonically by a one-variable phase equation that is coupled bi-directionally to a two-variable slow system. The model is analyzed in the slow-variable phase plane, using quasi steady-state assumptions and formal averaging. We derive a reduced system to explore where the full model exhibits bursting, steady-states, continuous and modulated spiking. The relative speed of activation and inactivation of the slow variables strongly influences the burst pattern as well as other dynamics. We find conditions of the bistability of solutions between continuous spiking and bursting. Although the phase model is simple, we demonstrate that it captures many dynamical features of more complex biophysical models.

**Key words:** Excitable membrane – Bursting oscillations – Neuronal modeling

### 1 Introduction

Some cells known as bursting pacemakers fire with a pattern that alternates between a silent phase of slowly changing membrane potential and an active

---

This research was partially supported by NSF-JOINT RESEARCH grant 8803573, grant from CONCYT and DGAPA(UNAM) Mexico for H. Carrillo, and for the S. M. Baer NSF DMS-9107538

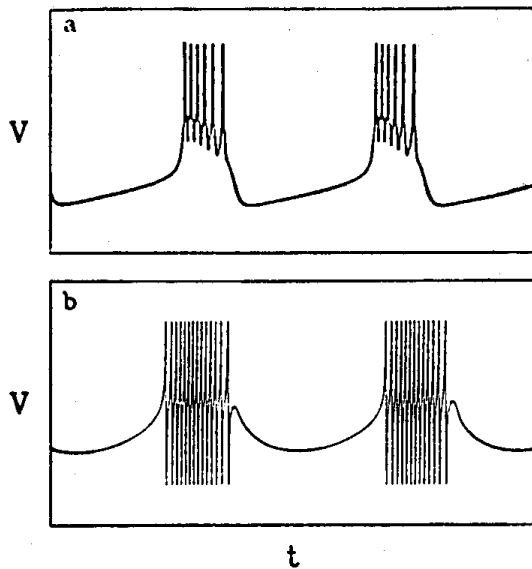


Fig. 1. Two kinds of burst patterns. **a** A square-wave burster computed using the Morris and Lecar model (from [24]); **b** A parabolic burst pattern generated from the phase-burster model (1)–(3) with parameter values  $\epsilon_x = 0.0050$ ,  $\epsilon_y = 0.0015$ ,  $a = 2$ ,  $b = 5$ ,  $I = -1.65$ ,  $p_x = -0.3$ ,  $p_y = -0.3$ , and  $V = \sin \theta(t)$

phase of repetitive spiking (see Fig. 1). Such activity has been observed experimentally in isolated neurons, in neuronal ensembles (e.g., central pattern generator networks for activation of rhythmic muscle contraction), and in secretory and muscle tissue [16]. Bursting requires at least two different time scales, one on the scale of slow modulations ( $10^{-1}$  to 10 s) and the other on the scale of individual action potentials (1 to 10 ms).

In this paper we formulate a tractable mathematical model for endogenous parabolic bursting to analyze transient and long-time behavior on both fast and slow time scales. Specifically, we couple a one-variable phase oscillator (or ring) model for fast spiking to a slow subsystem. We employ the method of averaging [28] to reduce the full model to an analytically accessible set of differential equations on the time scale of the slow oscillations. Although by averaging we lose the detailed time course of individual action potentials, we gain a biophysically meaningful description of the averaged effect of rapid spiking. Explicit averaging of rapid spikes in biophysical models has also been carried out in studies of neuronal ensembles where synaptic conductances vary slowly [25, 10].

Ring models follow the timing of individual action potentials (rather than their amplitude and shape) and have been used effectively to construct and analyze simplified models of excitable cells [33], coupled neural oscillators [30], reaction-diffusion systems [9], and parabolic burst activity (externally forced, to lowest order) [8]. Ring models track the phase angle  $\theta$  of each spike, so when there is repetitive spiking, as is the case during the active phase of a burst,  $\theta$  increases rapidly through multiples of  $2\pi$ . When repetitive activity ceases,  $\theta$  approaches a steady-state and for burst mechanisms this steady-state may be slowly varying.

We confine our study to endogenous parabolic bursters. A burster is called *endogenous* if the slow subsystem is coupled bi-directionally to (i.e., it affects and is affected by) the fast membrane dynamics. Endogenous bursters are unlike *follower* bursters which are driven by external forcing [24]. Mathematical models of endogenous bursting mechanisms are often modifications of the Hodgkin-Huxley model [17] with additional variables to account for the slowly modulated activity [23, 26, 19, 27].

Figure 1 shows two different types of endogenous burst patterns a square-wave burster (Fig. 1a) and a parabolic burster (Fig. 1b). The square-wave burster shows a relaxation-like character. The mean membrane potential jumps discontinuously when spiking begins and the spike frequency decreases at the end of active phase. This pattern is characteristic of electrical bursting activity observed in insulin-secreting  $\beta$ -cells of the islet of Langerhans in the pancreas [1]. There have been numerous Hodgkin-Huxley-type models exploring the biophysical mechanisms underlying bursting in  $\beta$ -cells and recently singular perturbation methods have been applied to this class of models [31, 22, 29]. The parabolic burster (Fig. 1b) rides on a smooth sinusoidal-like slow wave. The burst is called parabolic because the instantaneous spike frequency is low at both the beginning and end of an active phase. The R-15 neuron in the abdominal ganglion of *Aplysia* is an example of a parabolic burster and has been modeled by Plant [23] and studied qualitatively and numerically by others [26, 4, 5]. Parabolic bursting depends on there being at least two slow variables (for opposing effects: to promote or suppress rapid spike generation). In contrast, square-wave bursters need only one slow variable but with the requirement that the fast variable subsystem exhibit bistability [24].

This paper is organized as follows. Our model and some of its properties are described in Sect. 2. In Sect. 3 we derive the reduced system of equations and construct its nullclines in the slow-variable phase plane. In Sect. 4 we compare in the slow-phase plane trajectories generated by the phase burster with those generated by the reduced system. We find parameter regimes for bursting, steady states, pure slow waves, and continuous spiking. From the bifurcation structure of the reduced system we identify conditions for bistable solutions, modulated spiking, and more complex dynamics where formal averaging breaks down. Finally, in Sect. 5 we discuss in detail how the dynamics of the phase burster compares to a typical biophysical model for parabolic bursting. To facilitate this comparison we construct averaged nullclines for Rinzel and Lee's Ca-Ca model using a numerical procedure developed recently by Smolen et al. for a  $\beta$ -cell model [29].

## 2 Phase model for parabolic bursting

In our idealized phase oscillator model for endogenous parabolic bursting, we denote the two slow variables as  $x$  and  $y$ ;  $x$  activates and  $y$  depresses the fast spike generating process characterized by phase angle  $\theta$ . The phase burster

equations have the form

$$\frac{d\theta}{dt} = 1 - \cos \theta + A(x, y) \quad (1)$$

$$\frac{dx}{dt} = \varepsilon_x [x_\alpha(\theta) - x] \quad (2)$$

$$\frac{dy}{dt} = \varepsilon_y [y_\alpha(\theta) - y] \quad (3)$$

where  $\varepsilon_x, \varepsilon_y$  are parameters representing speed of activation and inactivation (usually of order less than one), and  $x_\alpha, y_\alpha$  are  $2\pi$ -periodic functions of  $\theta$  that strictly increase for  $-\pi/2 \leq \theta \leq 0$ . Unless otherwise specified we choose

$$x_\alpha(\theta) = \sin(p_x + \theta) \quad (4)$$

$$y_\alpha(\theta) = \sin(p_y + \theta) \quad (5)$$

where  $p_x$  and  $p_y$  are constants. We choose sinusoids to keep the model simple and analytic, but other forms are possible.

The slow subsystem, driven by  $\theta$ , feeds back to the fast subsystem to provide bi-directional coupling through the activation function  $A(x, y)$  defined by

$$A(x, y) = \tanh(ax - by + I), \quad (6)$$

where  $a > 0, b > 0$ . The net externally applied stimulus  $I$  is our primary control variable. Bursting occurs when the slow system (2–3) sweeps  $A(x, y)$  back and forth across  $A = 0$ . When  $-1 < A < 0$  (silent region),  $\theta$  is attracted to a slowly varying steady-state  $\theta_s$ . When  $0 < A < 1$  (active region), (1) destabilizes and  $\theta$  respectively increases with time scale  $O(1)$  through multiplies of  $2\pi$ , corresponding to repetitive spiking. As  $A$  decreases toward 0, the cycle time for  $\theta$  becomes infinite. The burst pattern shown in Fig. 1b is computed with (1)–(6), using  $\sin \theta$  to represent the membrane potential.

Figure 2 illustrates schematically how variations in the net stimulus  $I$  can lead to different responses. When there is strong inhibition there are no oscillations, the slow variables  $x, y$  and the fast variable  $\theta$  approach a stable steady-state (SSS). At the other extreme, strong excitation, there is continuous spiking (CS);  $x$  and  $y$  go to a steady-state, but  $\theta$  continuously increases through multiplies of  $2\pi$  ( $A > 0$ ). Bursting (B) is realized when the net stimulus induces a slow wave trajectory ( $x$  and  $y$  oscillations) that oscillates about  $A = 0$ . A pure slow wave (PSW) occurs when there is no spike activity; i.e., when  $A < 0$  during slow oscillations. Modulated spiking is characterized by frequency modulations.

The phase burster (1–3) is intended to be a simplified model, representative of a class of models for endogenous parabolic bursting. It is motivated by Rinzel and Lee's dissection of Plant's model for neuronal parabolic bursting [26]. We incorporate into our model the necessary dynamical features, identified from their analysis, that lead to parabolic burst activity. We neglect other

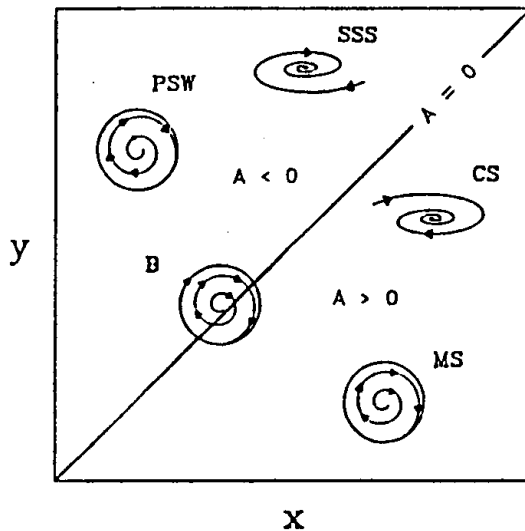


Fig. 2. Schematic representation of how bursting and other dynamics can be generated using the phase-burster model. The schematic shows the  $xy$ -phase plane divided by the line  $A = 0$ . The region  $A > 0$  corresponds to fast oscillations, the region  $A < 0$  is where  $\theta$  is steady or slowly changing. In  $A > 0$  CS denotes continuous spiking and MS modulated spiking. In  $A < 0$  PSW denotes periodic slow wave, and SSS stable steady state. Bursting B occurs when the slow variables approach a limit cycle that crosses back and forth across  $A = 0$ .

features in the more complex models which play a secondary role, to keep our model as simple as possible.

Figure 3a shows the time courses of  $V$ ,  $Ca$ , and  $x$  for a burst solution to Plant's model;  $Ca$  and  $x$  are the slow variables and  $V$ , representing membrane potential, is one of the fast variables. Biophysically,  $x$  is slow  $V$ -dependent activation of a calcium current (which turns on spiking) and  $Ca$  represents intracellular calcium concentration (governed by slow kinetics) which activates a potassium current (turning off spiking). The dynamics of bursting is dissected, mathematically, by first considering how the fast variable  $V$  changes when the slow variable  $Ca$  is treated as a static bifurcation parameter, while fixing  $x$ . Figure 3b is a bifurcation diagram showing a branch of periodic solutions emerging via a Hopf bifurcation at HB. This bifurcation is subcritical, so the emergent periodic orbits are unstable. The large amplitude orbits for  $Ca$  increasing beyond the knee are stable and they correspond to repetitive spiking. The periodic solution branch terminates at HC, with a homoclinic orbit at a saddle-node of fixed points. This termination structure (SNIC: saddle-node on an invariant circle) has co-dimension one and defines a curve in two-parameter space [15]. As  $Ca$  approaches HC the frequency of the periodic solutions approach zero. This transition boundary curve, HC, exists over the entire range of  $x$  (Fig. 3c).

Bursting oscillations occur when  $Ca$  and  $x$  are dynamic slow variables that sweep back and forth across the HC boundary (see Fig. 3c). When the trajectory generated by the slow subsystem is above HC the fast subsystem has a stable limit cycle. When it intersects the transition boundary a saddle node is created, and as the trajectory passes below HC a stable node splits off the saddle node causing the spike activity to cease as  $V$  relaxes and following the slowly varying steady-state  $V_{ss}(x, Ca)$ . Spiking drives  $Ca$  upward with the effect of slowly depressing the system until the activation variable  $x$  relaxes quickly to a lower value. Repetitive spiking ceases since the  $(Ca, x)$  trajectory

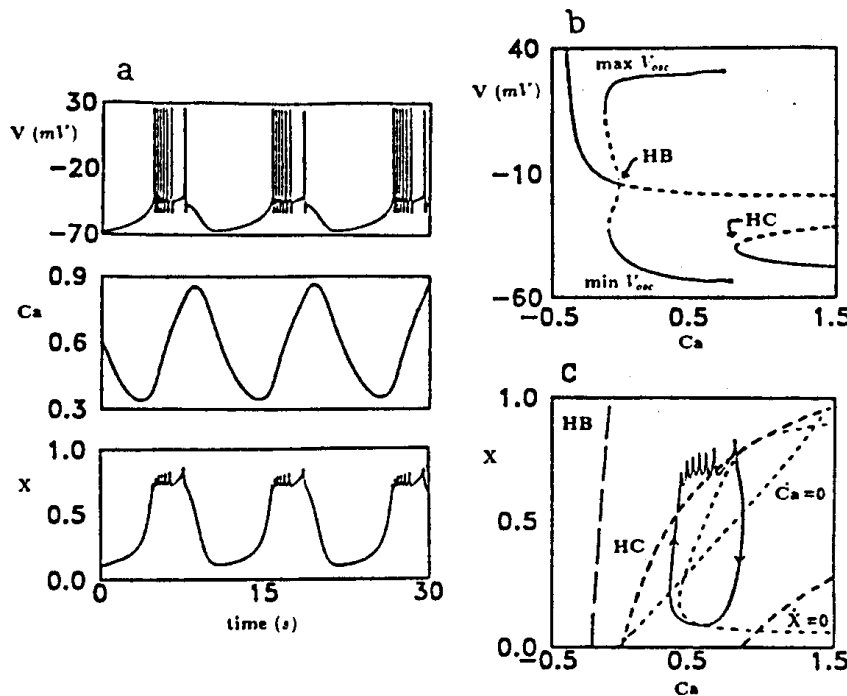


Fig. 3. The dissection of a biophysical model for parabolic bursting. From Rinzel and Lee [26]. **a** Time courses of  $V$ ,  $Ca$  and  $x$  for a burst solution to Plant's model. **b** Bifurcation diagram of  $V$  versus  $Ca$  for  $x$  fixed ( $x = 0.7$ ). HB denotes a Hopf bifurcation and HC a homoclinic bifurcation. **c** A two parameter bifurcation study of the same model. HC separates the active and silent regions, playing the same role as the line  $A = 0$  in the phase burster model (see Fig. 2); the slow trajectory exhibits oscillations only on one side of the HC boundary

falls below HC. However, after cessation of repetitive activity,  $Ca$  starts decreasing slowly until the trajectory crosses above HC due to a re-triggering of the activation variable  $x$ . Note that the Hopf boundary HB is not directly involved in the burst dynamics, and therefore plays a secondary role. We discard this feature in our formulation of the phase model.

The phase burster is essentially a canonical representation of these autonomous interactions among variables. The fast system is characterized using ring dynamics (see Fig. 4). Bursting oscillations occur when the slow variables  $x$  and  $y$  cause the activation function  $A(x, y)$  to sweep back and forth across  $A = 0$ . When  $A$  is positive the phase angle  $\theta$  on the ring (see Fig. 4a) increases through multiples of  $2\pi$ , corresponding to repetitive spiking. When  $A$  is zero, saddle nodes exist at multiples of  $2\pi$  in (1) (see Fig. 4b), and for  $A$  negative there are two singular points for each multiple of  $2\pi$ ; a stable node and a saddle node (Fig. 4c). When  $A$  is negative,  $\theta$  tracks a slowly varying stable manifold given by  $\theta_s(x, y)$ . As for this ring model, the detailed models have an invariant circle in phase space which persists across the HC boundary; on one side of HC, there is a pair of fixed points (saddle and node) on the circle.

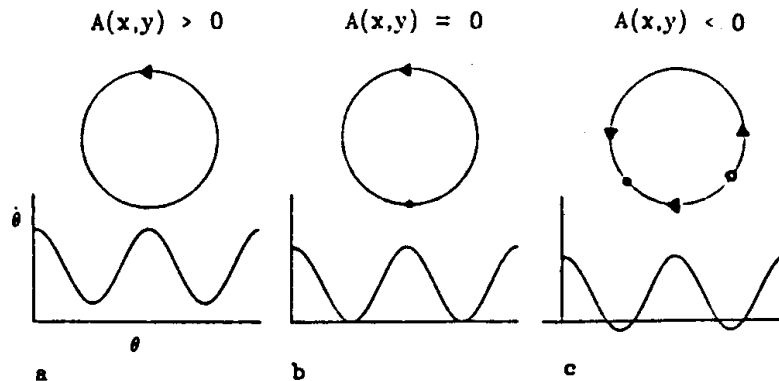


Fig. 4. The fast subsystem is governed by ring dynamics. The curves plot the right hand side of (1) over two periods ( $4\pi$ ). The rings represent the dynamics of  $\theta$  for the three cases  $A$  positive, zero, and negative. Recall that  $A$  is coupled bi-directionally to  $\theta$  through  $x$  and  $y$ . **a** When  $A(x, y) > 0$ ,  $d\theta/dt$  is always positive. The phase  $\theta$  increases through multiples of  $2\pi$  on the ring, corresponding to fast oscillations. **b** The case  $A(x, y) = 0$  is analogous to a homoclinic bifurcation boundary (see Fig. 3c). **c** When  $A(x, y) < 0$ , the phase  $\theta$  has two singular points every  $2\pi$ , one stable and the other unstable;  $\theta$  slowly tracks the stable one (moduli  $2\pi$ ) as  $x$  and  $y$  slowly change

The slow and fast subsystems of the phase burster are bi-directionally coupled. When the slow system has disparate time scales ( $\epsilon_x \ll \epsilon_y$  or  $\epsilon_y \ll \epsilon_x$ ) slow waves may behave like relaxation oscillators. It is easy to see from an inspection of the activation function (6) that  $x$  activates and  $y$  depresses the fast subsystem; the sigmoidal form of the hyperbolic tangent acts as a switch that activates the fast subsystem. On the other hand, the slow system cannot oscillate without variations in  $\theta$ . Thus the slow system drives the fast and the fast drives the slow, as in biophysical models for parabolic bursting.

Figure 5 shows the time course of  $\sin \theta$ ,  $y$  and  $x$  for a burst solution to (1–3);  $\sin \theta$  behaves like  $V$  and the slow variables,  $y$  and  $x$ , behave like  $Ca$  and  $x$  (in Fig. 3a), respectively. Although the phase burster is a simple model, it captures many dynamical features of more complex models (compare Fig. 3a to Fig. 5).

Computations in this paper were performed on a VAX 8600 using both Gear's method [12] and a classical fourth-order Runge Kutta method [13]. Preliminary calculations made extensive use of G.B. Ermentrout's program PHASEPLANE [7], and another phase plane analysis tool called INTEGRA developed at the Universidad Nacional Autonoma de Mexico. Bifurcation diagrams were constructed using Runge-Kutta with vectorization over the range of the bifurcation parameter; a time step of  $10^{-2}$  was used in the silent regions and  $10^{-3}$  in the active regions. AUTO [6] was used as a check and also to compute unstable and homoclinic points of bifurcation, as well as limit points. Gear's method was used for calculations of parabolic bursting for Rinzel and Lee's [26] Ca-Ca model. We construct the averaged nullclines in Fig. 12 using a method recently developed by Smolen et al [29], in which

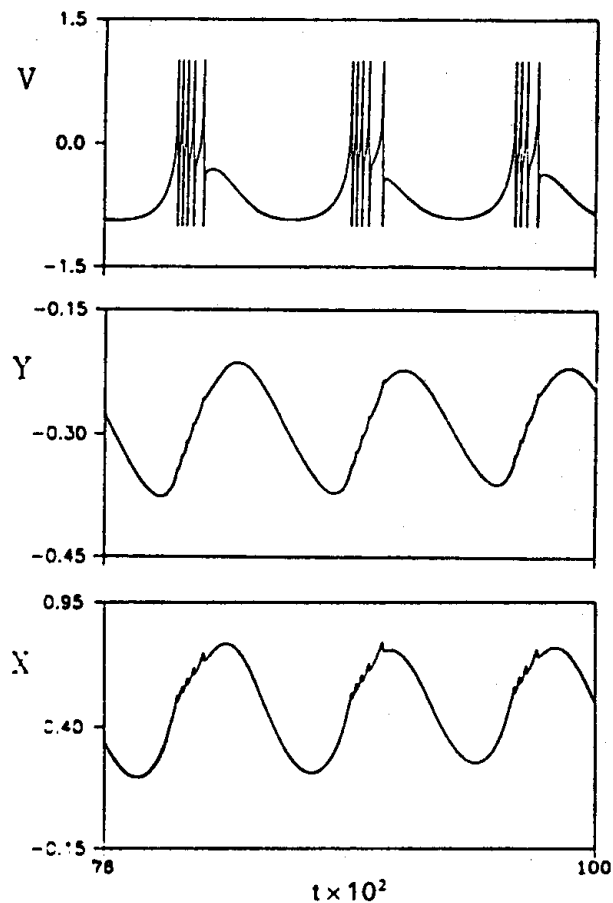


Fig. 5. A burst solution to the phase model. Time course of  $V = \sin \theta$ ,  $y$  and  $x$ . Here  $x_\alpha$  and  $y_\alpha$  are represented by sine functions (see (4) and (5));  $\epsilon_x = 0.01$ ,  $\epsilon_y = 0.0012$ ,  $a = 2$ ,  $b = 5$ ,  $I = -2.74$ ,  $p_x = 1.3$ ,  $p_y = 0.4$ . The burst solutions are qualitatively similar to Plant's model (compare Fig. 3a)

AUTO finds nullclines for the slow variables when the fast variables are periodic by averaging over the fast oscillations. This numerical procedure is not needed for the phase burster model since we can derive the averaged equations explicitly.

### 3 The reduced system and its phase plane structure

In this section we reduce the dynamics of (1)–(3) to the slow-variable phase plane by exploiting disparities in time scales between fast and slow subsystems. We derive equations for when the fast system settles into a quasi-steady-state ( $A < 0$ ). Finally, we characterize analytically the structure of the  $x$  and  $y$  nullclines in the phase plane.



For  $A < 0$ , (1) has two equilibrium points,  $\theta_s$  and  $\theta_u$ , one stable and the other unstable. They are given by

$$\theta_u = + \arccos(1 + A(x, y)) \quad (7)$$

$$\theta_s = - \arccos(1 + A(x, y)) . \quad (8)$$

where the range of arccosine is restricted to  $(0, \pi/2)$  since  $-1 < A < 0$ , and therefore  $-\pi/2 < \theta_s < 0$  and  $0 < \theta_u < \pi/2$ . The function  $\theta_s(x, y)$  constitutes a stable two dimensional slow manifold of the system [32]. For  $A < 0$ , solutions to (1-3) rapidly approach this manifold, at least to leading order in  $\varepsilon_x$  and  $\varepsilon_y$  [18]. The slow trajectory  $(x, y)$  in the silent region is given by the quasistatic approximation

$$\frac{dx}{dt} = \varepsilon_x [x_x(\theta_s(x, y)) - x] \quad (9)$$

$$\frac{dy}{dt} = \varepsilon_y [y_x(\theta_s(x, y)) - y] . \quad (10)$$

For  $A > 0$ , the slow dynamics in the oscillatory region, derived from formal averaging, is governed by

$$\frac{dx_{av}}{dt} = \varepsilon_x [\bar{x}_x(A(x_{av}, y_{av})) - x_{av}] \quad (11)$$

$$\frac{dy_{av}}{dt} = \varepsilon_y [\bar{y}_x(A(x_{av}, y_{av})) - y_{av}] . \quad (12)$$

where,

$$\bar{x}_x(A) = \frac{1}{T(A)} \int_0^{2\pi} \frac{x_x(\theta)}{1 - \cos \theta + A} d\theta \quad (13)$$

$$\bar{y}_x(A) = \frac{1}{T(A)} \int_0^{2\pi} \frac{y_x(\theta)}{1 - \cos \theta + A} d\theta . \quad (14)$$

Here  $T$  is the slowly varying period, found by integrating (1) from  $\theta = 0$  to  $2\pi$ , while holding  $A$  fixed:

$$\begin{aligned} T(A) &= \int_0^{2\pi} \frac{d\theta}{1 - \cos \theta + A} \\ &= \frac{2\pi}{\sqrt{(A+1)^2 - 1}} . \end{aligned} \quad (15)$$

We obtain closed form expressions for  $\bar{x}_x(A)$  and  $\bar{y}_x(A)$ , using the sine model for  $x_x$  and  $y_x$ . Substituting (4) and (5) into (13) and (14), respectively we have after integrating

$$\bar{x}_x = \sin p_x [(A+1) - \sqrt{(A+1)^2 - 1}] \quad (16)$$

$$\bar{y}_x = \sin p_y [(A+1) - \sqrt{(A+1)^2 - 1}] . \quad (17)$$

Together, the quasi-static (9)–(10) and averaged equations (11)–(12), constitute the reduced system for the phase burster (1)–(3). Its solutions are continuous and differentiable for  $A \neq 0$ . As  $A \rightarrow 0$  the component systems match asymptotically (compare (16)–(17) for  $A = 0$  with (4)–(5) for  $\theta = 0$ ). To verify this in general, substitute (15) into (13) and (14); for  $\bar{x}_x$ , we have

$$\bar{x}_x(A) = \frac{1}{2\pi} \int_0^{2\pi} \frac{x_x(\theta) \sqrt{(1+A)^2 - 1}}{1 - \cos \theta + A} d\theta. \quad (18)$$

Note that the integrand approaches zero for small positive  $A$  everywhere except near  $\theta = 0$  and  $\theta = 2\pi$ . Near these endpoints  $x_x(\theta) \sim x_x(0)$ , since  $x_x(\theta)$  is  $2\pi$  periodic and well behaved. Therefore, as  $A \rightarrow 0^+$ , we can replace  $x_x(\theta)$  by  $x_x(0)$  in (18) and integrate again using (15). After simplifying, we obtain  $\bar{x}_x(A) \sim x_x(0)$  as  $A \rightarrow 0^+$ . Similarly,  $\bar{y}_x(A) \sim y_x(0)$  as  $A \rightarrow 0^+$ .

The reduced system can be studied in the phase plane since its constituent subsystems are each second-order. The  $x$ -nullcline is the set of points in the  $xy$ -plane where the solution trajectories are vertical ( $\dot{x} = 0$ ) or vanish. The  $y$ -nullcline is the set of points where the trajectories are horizontal ( $\dot{y} = 0$ ) or vanish. We denote  $\dot{x} = 0$  to be the part of the  $x$ -nullcline that lies in the silent region and  $\dot{x}_{\text{osc}} = 0$ , the  $x_{\text{osc}}$ -nullcline, the part that lies in the oscillatory region. Likewise, we distinguish the two portions of the  $y$ -nullcline as  $\dot{y} = 0$  and  $\dot{y}_{\text{osc}} = 0$ . The nullclines are smooth curves for  $A \neq 0$ . At points where  $A = 0$  the nullclines are continuous but not necessarily smooth. Continuity of the nullclines is assured at  $A = 0$  since both  $\bar{x}_x(A)$  and  $\bar{y}_x(A)$  are asymptotic to  $x_x(0)$  and  $y_x(0)$  respectively, as  $A$  approaches zero.

The  $x$ -nullcline in the silent region ( $-1 < A < 0$ ) is a function of  $x$  and is found by setting the right side of (9) to zero. We can characterize the  $x$ -nullcline analytically using the following parameterization:

$$x(\theta_s) = x_x(\theta_s) \quad (19)$$

$$y(\theta_s) = \frac{1}{b} [a x_x(\theta_s) + \frac{1}{2} \ln(2 \sec \theta_s - 1) + I], \quad (20)$$

where  $-\pi/2 < \theta_s < 0$  from (8). The  $y$ -coordinate (20) is found by solving for  $y$  in terms of  $x$  in (6) using the log equivalent of the inverse hyperbolic tangent ( $\tanh^{-1} A = \frac{1}{2} \ln((1+A)/(1-A))$ ), and then replacing  $A$  by its quasi-static approximation ( $\cos \theta_s - 1$ ), found by solving for  $A$  in (1) after setting  $d\theta/dt = 0$ .

The derivative of the  $x$ -nullcline is then

$$\frac{dy}{dx} = \frac{a}{b} \left[ 1 + \frac{\tan \theta_s}{a(2 - \cos \theta_s) x'_x(\theta_s)} \right], \quad (21)$$

where  $x'_x(\theta_s) > 0$  since  $x_x$  is strictly increasing over the domain of  $\theta_s$ . As  $x$  increases from  $x_x(-\pi/2)$ , the  $x$ -nullcline decreases from its vertical asymptote, reaches a minimum, and then eventually increases until it approaches tangentially the line  $A = 0$ , at the point  $(x_x(0), a/b x_x(0) + I/b)$ . If  $x''_x(\theta_s) > 0$ , then it is easy to show that  $y''(x) > 0$ . For this case the  $x$ -nullcline is a U shaped

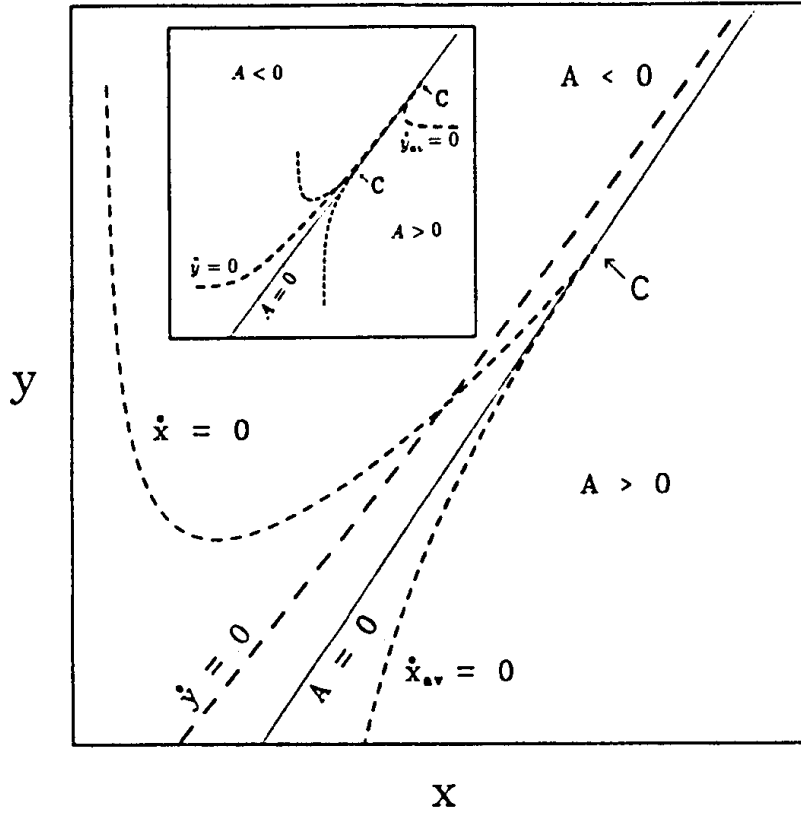


Fig. 6. Nullclines and curve  $A(x, y) = 0$  in the  $xy$  phase plane. The silent region is  $A < 0$  and the active region is  $A > 0$ . The  $x$  and  $y$  nullclines are computed from the quasi-static approximation given by (9)–(10) for  $A < 0$ , and the averaged approximation (11)–(12) for  $A > 0$ . The inset is a rescaled view showing both  $y$ -nullclines. The equation of the line  $A = 0$  is  $ax - by + I = 0$ . The  $x$  nullclines converge at  $C$ , on the line  $A = 0$ , and form a cusp. The  $y$ -nullclines also form a cusp, as shown in the inset. Parameter values are the same as in Fig. 5 and Fig. 7c

curve that *monotonically* decreases from infinity, reaches a minimum value and then increases *monotonically* until it touches the line  $A = 0$ . The sine model (4)–(5) satisfies this condition and its  $x$ -nullcline is U shaped as shown in Fig. 6.

The structure of the  $y$ -nullcline in the silent region can also be determined from a parametric representation:

$$x(\theta_s) = \frac{1}{a} [b y_x(\theta_s) - \frac{1}{2} \ln(2 \sec \theta_s - 1) - I] \quad (22)$$

$$y(\theta_s) = y_x(\theta_s) \quad (23)$$

The  $y$ -nullcline is an increasing function of  $x$  in the silent region since

$$\frac{dy}{dx} = \frac{a}{b} \left[ 1 - \frac{\tan \theta_s}{b(2 - \cos \theta_s) y'_x(\theta_s)} \right]^{-1} > 0 \quad (24)$$

Therefore, the  $y$ -nullcline rises (shown in Fig. 6 inset) from a horizontal asymptote until it approaches tangently the line  $A = 0$  at the point  $(b/a y_x(0) - I/a, y_x(0))$ .

Similarly, in the active region ( $0 < A < 1$ ), the  $x_{av}$ -nullcline can be characterized analytically by first setting the right side of (11) to zero and then parameterizing as follows:

$$x_{av}(A) = \bar{x}_x(A) \quad (25)$$

$$y_{av}(A) = \frac{1}{b} \left[ a \bar{x}_x(A) - \frac{1}{2} \ln \left( \frac{1-A}{1+A} \right) + I \right] \quad (26)$$

once again utilizing (6) and the relation  $\tanh^{-1} A = \frac{1}{2} \ln((1+A)/(1-A))$ .

In order to satisfy the required condition that  $x_x(\theta)$  and  $y_x(\theta)$  are increasing functions on  $(-\pi/2, 0)$  we assume for the sine model that  $p_x, p_y \in (0, \pi/2)$ . This requirement for  $A > 0$  implies that both  $\bar{x}'_x(A)$  and  $\bar{y}'_x(A)$  are negative, which becomes evident after differentiating (16) and (17).

The derivative of the  $x_{av}$ -nullcline in the oscillatory region is then

$$\frac{dy_{av}}{dx_{av}} = \frac{a}{b} \left[ 1 - \frac{1}{a(1-A^2)\bar{x}'_x(A)} \right] \quad (27)$$

where, for the sine model

$$\bar{x}'_x(A) = \sin p_x \left[ 1 - \frac{A+1}{\sqrt{(A+1)^2 - 1}} \right] < 0. \quad (28)$$

Therefore, as  $A$  decreases from  $A = 1$ , the  $x_{av}$ -nullcline increases monotonically from its vertical asymptote as shown in Fig. 6 (inset). It continues to rise until it becomes tangent to the line  $A = 0$  where it is continuous, as expected, with the  $x$ -nullcline from the silent region.

The  $y_{av}$ -nullcline has the parametric form

$$x_{av}(A) = \frac{1}{a} \left[ b \bar{y}_x(A) + \frac{1}{2} \ln \left( \frac{1+A}{1-A} \right) - I \right] \quad (29)$$

$$y_{av}(A) = \bar{y}_x(A) \quad (30)$$

where  $\bar{y}_x$  is a decreasing function given by (17) above. The derivative of the  $y_{av}$ -nullcline in the oscillatory region is then

$$\frac{dy_{av}}{dx_{av}} = \frac{a}{b} \left[ 1 + \frac{1}{b(1-A^2)\bar{y}'_x(A)} \right]^{-1} \quad (31)$$

where, for the sine model

$$\bar{y}'_x(A) = \sin p_y \left[ 1 - \frac{A+1}{\sqrt{(A+1)^2 - 1}} \right] < 0. \quad (32)$$

As  $A$  approaches zero,  $\bar{y}'_x$  approaches negative infinity and therefore (31) approaches the slope  $a/b$  through positive values. Again, as expected, the

$y_{\text{act}}$ -nullcline is continuous with its counterpart emerging from the silent region. As  $A$  nears one, the nullcline approaches a horizontal asymptote from above. Within the interval  $0 < A < 1$ , (31) is never zero but can change sign. Therefore, the  $y_{\text{act}}$ -nullcline may have at least one vertical asymptote (see  $\dot{y}_{\text{act}} = 0$  in Fig. 6 inset).

The complete set of nullclines and the line  $A = 0$  (for the sine model) are drawn and labeled in the inset of Fig. 6. The  $x$  and  $y$  nullclines, on both sides of  $A = 0$ , converge continuously into cusps (denoted by  $C$  in the figure) terminating on the line  $A = 0$ . An intersection of  $x$  and  $y$  nullclines corresponds to a steady-state solution; in Fig. 6, the nullclines intersect in the silent region  $A < 0$ .

The phase plane structure in Fig. 6 is consistent with the schematic slow-variable phase plane described in Fig. 2. A stable steady-state in  $A < 0$  corresponds to a stable steady-state of the full system, but a stable steady-state in  $A > 0$  corresponds to continuous spiking. A limit cycle confined to the region  $A < 0$  is a periodic slow wave and a limit cycle entirely in region  $A > 0$  is modulated spiking. Bursting is a limit cycle that traverses back and forth across  $A = 0$ . In the next section we integrate both the full and reduced equations and superimpose their solution trajectories in the slow-phase plane.

#### 4 Phase burster dynamics

We now analyze the phase burster in the slow phase plane and determine critical parameter values for bursting, pure slow waves, continuous spiking, steady-states, and modulated spiking. We will show that the reduced system (9)–(10) has dynamics similar to other two variable models of excitability, such as the FitzHugh-Nagumo [11] and Morris-Lecar [21] equations; e.g., super and subcritical Hopf bifurcations, saddle nodes, and intervals of repetitive activity. Furthermore, when  $\varepsilon_y \ll \varepsilon_x$  or vice versa, the reduced system has singular behavior and relaxation oscillator properties [20, 14]. We use the reduced system to determine parameter values for the values for the full model that bracket lower and upper thresholds for bursting, steady states, continuous and modulated spiking. We also find conditions for bistability of solutions between continuous spiking and bursting.

We begin our analysis by studying solution trajectories in the phase plane. Figure 7a–d compares computed solution trajectories for both the full and reduced systems for  $\varepsilon_y \ll \varepsilon_x$ . The nullclines and the line  $A = 0$  are labeled in Fig. 6. Figure 7 trajectories for the reduced system (dashed) track closely the trajectories for the full system (solid), except trajectory 2 in Fig. 7a, where they move slightly apart after entering the silent region.

Figure 7a illustrates the case of a stable steady-state in the silent region ( $A < 0$ ). Trajectory 1, initiated in the silent region, spirals into the fixed point located where the  $x$  and  $y$  nullclines intersect. There are no fast oscillations since the trajectory's path lies entirely in the silent region. However, trajectory 2 emerging from the active region, has small oscillations as it passes upward

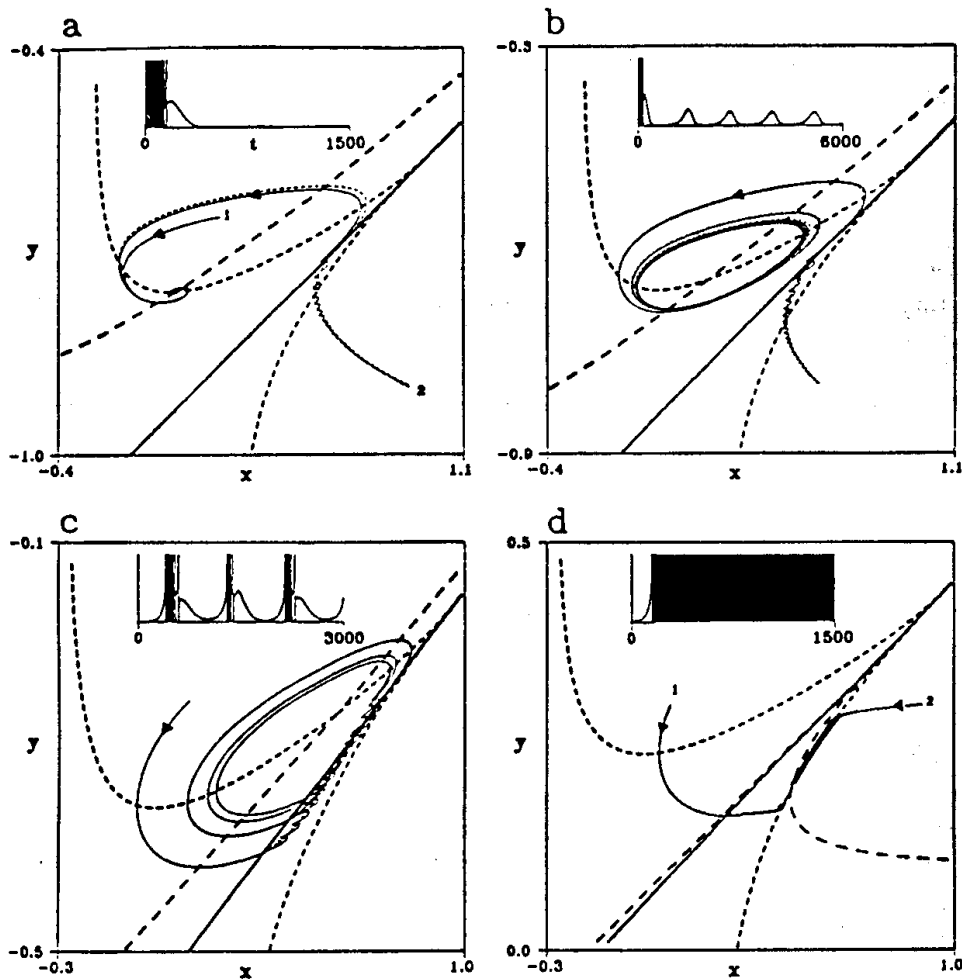


Fig. 7. Dynamical features of the phase burster model for  $\varepsilon_y \ll \varepsilon_x$ . Except for  $I$ , the parameter values are the same as in Fig. 5. Trajectories of the full (solid) and reduced (short dashed) systems are in good agreement for the chosen parameters. Compare this figure with Fig. 2 and the bifurcation diagram in Fig. 8. **a**  $I = -4.74$ : Two trajectories, 1 and 2, initiated on opposite sides of the line  $A = 0$  both converge to a steady-state in the silent region. The time course for trajectory 2 is displayed in the inset. Initial conditions are  $(0.2, -0.65)$  and  $(0.9, -0.9)$  for trajectories 1 and 2, respectively. This value of  $I$  corresponds to SSS in Fig. 2 and case a in the bifurcation diagram of Fig. 8. **b**  $I = -4.24$ : A single trajectory initiating at  $(0.6, -0.8)$  in the active region approaches a limit cycle entirely in the silent region. The time course settles into a periodic slow wave (PSW in Fig. 2 and case b in Fig. 8). **c**  $I = -2.74$ : The trajectory from  $(0.120, -0.256)$  approaches a bursting solution: case c in Fig. 8 and B in Fig. 2. This case is identical to Fig. 5. **d**  $I = 0.26$ : Trajectories are initiated on opposite sides of  $A = 0$ , but both converge to a steady-state in the active region, which corresponds to the continuous spiking case CS in Fig. 2 and d in Fig. 8. Initial conditions are  $(0.9, 0.3)$  and  $(0.1, 0.3)$ . The time course of trajectory 1 is shown in the inset

and vertically over the  $x_{at}$ -nullcline. The trajectory crosses into the silent region nearly tangent to  $A = 0$  before spiraling counterclockwise into the fixed point. The time course of trajectory 2, shown in the inset, exhibits repetitive spikes that decrease in frequency just prior to settling into steady-state.

The trajectories shown in Fig. 7b are initiated in the active region and approach a limit cycle confined to the silent region. The time course starts with rapid spiking, but then quickly settles into pure slow waves with “saw-tooth” oscillations, a characteristic feature of small amplitude oscillations [2].

Figure 7c illustrates burst activity. The counterclockwise trajectory is nearly tangent to the line  $A = 0$  before leaving the oscillatory region. Consequently the period  $T(x, y)$  increases just at the end of each active phase. This feature is displayed in the inset to Fig. 7c, which shows a burst solution to the full problem for these same parameter values. The last few spikes of each active phase shows a marked decrease in spike frequency. Also observe that these bursts ride on slow oscillations which is characteristic of a bursting pacemaker neuron, and  $\sin \theta$  is nearly zero at the beginning and end of the active phase.

In Fig. 7d, both trajectories 1 and 2 approach a fixed point where the  $x_{ar}$  and  $y_{ar}$  nullclines intersect. Continuous spiking results, since  $A > 0$ . Trajectory 1 (time course in inset) starts in the silent region and then converges to a fixed point in the active region. Trajectory 2 starts in the oscillatory region and converges to the same fixed point.

The bifurcation structure of the reduced system, for  $\varepsilon_y \ll \varepsilon_x$ , is shown in Fig. 8. The net stimulus  $I$  is chosen as the primary control parameter. At the lower range of the net stimulus ( $I = -6$ ), the activation function is in the silent region ( $A < 0$ ). Solution trajectories converge to a stable steady state (SSS) there. The values of  $I$  indicated by a–d in the figure correspond to the parameter settings for Fig. 7a–d.

There is a (supercritical) Hopf bifurcation to periodic solutions at HB ( $I \doteq -4.42$ ). Here, the activation function is negative, so the full system exhibits pure slow waves PSW (c.p., Fig. 7b). The periodic branch is near vertical due to the disparate time scales of the slow system. Consequently, for  $I$  just to the right of HB the slow waves have small amplitude relaxation oscillator properties, such as the sawtooth wave pattern in Fig. 7b inset (see Baer and Erneux [2, 3] for an analysis of two-variable singular Hopf bifurcations to relaxation oscillations). For larger values of  $I$  the activation function continues to oscillate but sweeps positive for a fraction of its period (see inset), which corresponds to bursting in the full model (c.p., Fig. 7c). The dashed curve B is the fraction of time that the burst solution spends in the active phase (use same scale as  $A$ ); time spent in the active phase increases as  $I$  increases.

Over the interval  $-2 < I < 0$  the activation function spends much of its time in the vicinity of  $A = 0$ , and the leading order estimate given by averaging breaks down (In cases where the slow trajectory remains near a SNIC curve, like  $A = 0$ , one could apply the analytic method developed by Ermentrout [10] to approximate the slow trajectory.) Numerical solutions of the full system in this domain have complicated dynamics; as  $I$  approaches zero (the cusp) bursting and spiking become irregular. Hodgkin-Huxley like bursting models exhibit a similar transitional behavior (see Discussion). Finally, for  $I$  positive, the system spikes continuously CS (c.p., Fig. 7d). The horizontal

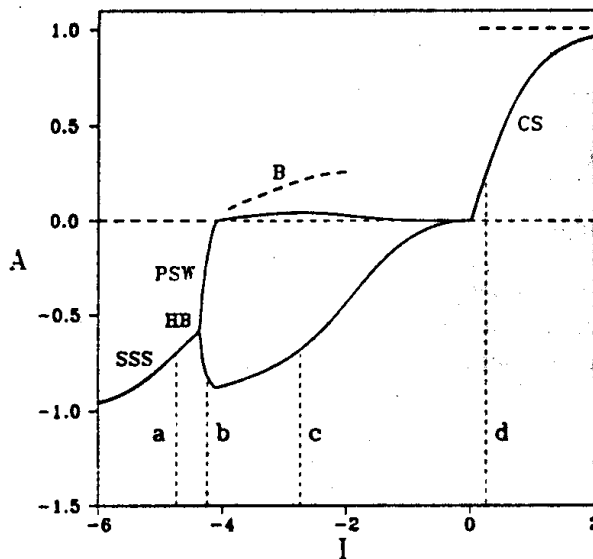


Fig. 8. Bifurcation structure of the phase for  $\varepsilon_y \ll \varepsilon_x$ , computed from reduced system: (9)–(10) and (11)–(12). Parameter values with the exception of  $I$  are given in Fig. 5. The figure shows that as the static values of  $I$  increase, the system undergoes a Hopf bifurcation at HB from a stable steady-state SSS to periodic slow waves PSW, and then a transition to bursting B followed eventually, for large values of  $I$ , by continuous spiking CS. The long dashed curve indicates the domain of  $I$  over which the reduced system exhibits organized bursting. The long dashed curve also indicates the fraction of a burst period that the system is in the active phase (use same scale as  $A$ ). The curve is not continued in the vicinity of the cusp since the reduced system is not reliable there. The values of  $I$  denoted by a–d correspond to Fig. 7a–d

dashed line above the CS curve indicates that the system eventually spends all its time in the active phase.

When  $\varepsilon_x \ll \varepsilon_y$  the bifurcation structure is quite different. Instead of a Hopf bifurcation from SSS to PSW, Fig. 9 shows that the system apparently goes directly from SSS to B through a homoclinic bifurcation. The dashed curve labeled UCS is an unstable steady-state branch, which corresponds to a branch of unstable continuous spiking solutions for the full system. At large stimulus values, the reduced system has a stable steady-state, therefore the full system spikes continuously. Unlike Fig. 8, there is a Hopf bifurcation for  $A > 0$  rather than for  $A < 0$ . Just to the right of HB two kinds of stable solutions coexist a stable steady-state and a large amplitude periodic solution. The stable steady-state corresponds to continuous spiking and the stable periodic solution corresponds to bursting, since  $A$  alternates sign each cycle (see Fig. 11a and b, respectively). The bifurcation is subcritical, so the local periodic branch is unstable, and periodic solutions on this branch correspond to unstable modulated spiking UMS in the full system (see Fig. 11c). In this bifurcation structure there are no values for  $I$  that give rise to stable slow waves. To obtain stable modulated spiking would require a supercritical Hopf



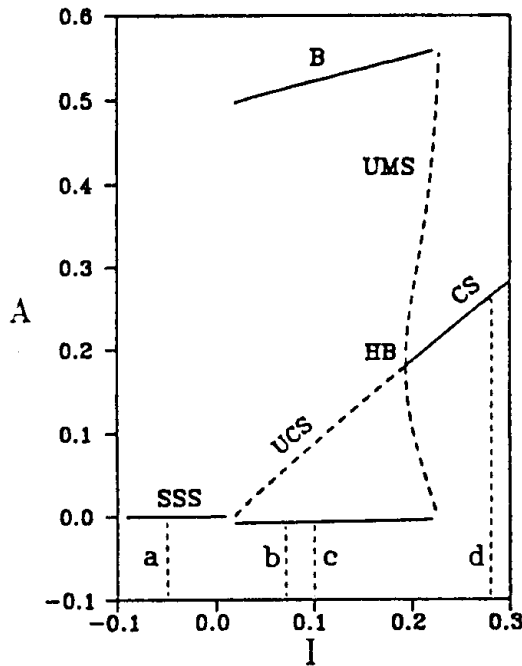


Fig. 9. Bifurcation structure of the phase burster for  $\varepsilon_x \ll \varepsilon_y$ . Parameter values the same as in Fig. 8, except  $\varepsilon_x = 0.002$  and  $\varepsilon_y = 0.008$ . Bifurcation diagram predicts stable steady states (SSS) for the full system if  $I$  negative or small positive. For large values of  $I$  (here,  $I > 0.2$ ) the reduced system predicts continuous spiking (CS), but changes stability through a Hopf bifurcation (HB) near  $I = 0.2$ . The periodic solutions to the left of the Hopf point correspond to bursting (B), since  $A$  changes sign repetitively. The dashed curve labeled UMS is an unstable periodic branch of the reduced system. This subcritical branch corresponds to unstable modulated spiking (UMS), since  $A > 0$ . Furthermore, the subcritical structure implies bistable behavior for  $I$  just to the right of HB (Fig. 11). The other dashed curve is an unstable steady-state of the reduced system for  $A > 0$  and corresponds to unstable continuous spiking (UCS). The values of  $I$  denoted by a–d are used in Fig. 10

bifurcation for  $A > 0$ . A local bifurcation analysis (not provided here) of the averaged subsystem (11)–(12) demonstrates that the bifurcation is always subcritical. Consequently, for our model in its present form, there are no stable solutions exhibiting modulating spiking. We note that coexistence of bursting and continuous spiking behavior has also been found in a parabolic burster model by Canavier et al [4].

The dynamics of the solution trajectories for  $\varepsilon_x \ll \varepsilon_y$  also differ significantly from those shown in Fig. 7. Panels a–d in Fig. 10 correspond to the values of  $I$  labeled in Fig. 9. First observe that the trajectories are clockwise rather than counterclockwise as they were in Fig. 7, and the time scales of the burst solutions are much longer. In Fig. 10a the nullclines intersect in the silent region very near  $A = 0$ . Consequently, a trajectory initiated in the oscillatory region moves upward, but unlike in Fig. 7a it is forced to follow parallel and close to the line  $A = 0$ . Figures 10b and c have nearly identical nullclines, since

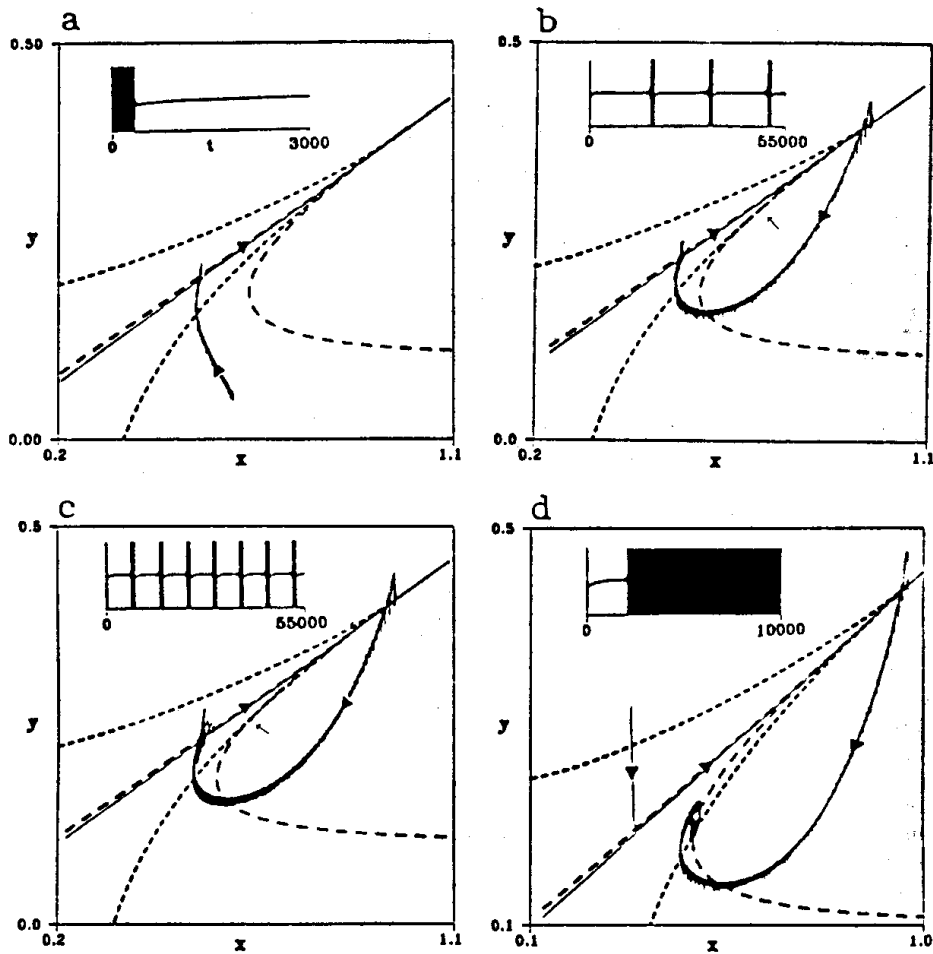


Fig. 10. Dynamical features of the phase burster model for  $\varepsilon_x \ll \varepsilon_y$ . Parameter values the same as in Fig. 9 and  $I$  values correspond to a–d in that figure. **a**  $I = -0.05$ : a trajectory initiated in the oscillatory region converges to a steady-state in the silent region. The time course ( $\sin \theta$  vs.  $t$ ) is shown in the inset. **b**  $I = 0.07$ : a burst solution with a long silent phase. This stimulus value is near the homoclinic bifurcation point where bursting emerges from a stable steady-state (see Fig. 9). The trajectory is near  $A = 0$ , during the silent phase, which explains why  $\sin \theta$  is approximately zero. The small arrow denotes where nullclines intersect. **c**  $I = 0.10$ : away from the homoclinic onset of bursting the silent phase is shorter, although the nullclines change orientation very little. **d**  $I = 0.28$ : a trajectory initiated in the silent phase drops to the  $y$ -nullcline, follows parallel to  $A = 0$ , then crosses into the oscillatory region at the cusp and spirals into a steady-state. The steady-state corresponds to continuous spiking (see inset)

$I$  differs only slightly. Even their phase plane trajectories are nearly identical. However, an examination of the time course (inset) shows a distinct difference between these two figures. The silent phase in Fig. 10b is over twice as long as that in Fig. 10c. This longer silent phase is due to the fact that  $I$  is closer to a homoclinic point of bifurcation than in Fig. 10c. This feature can be

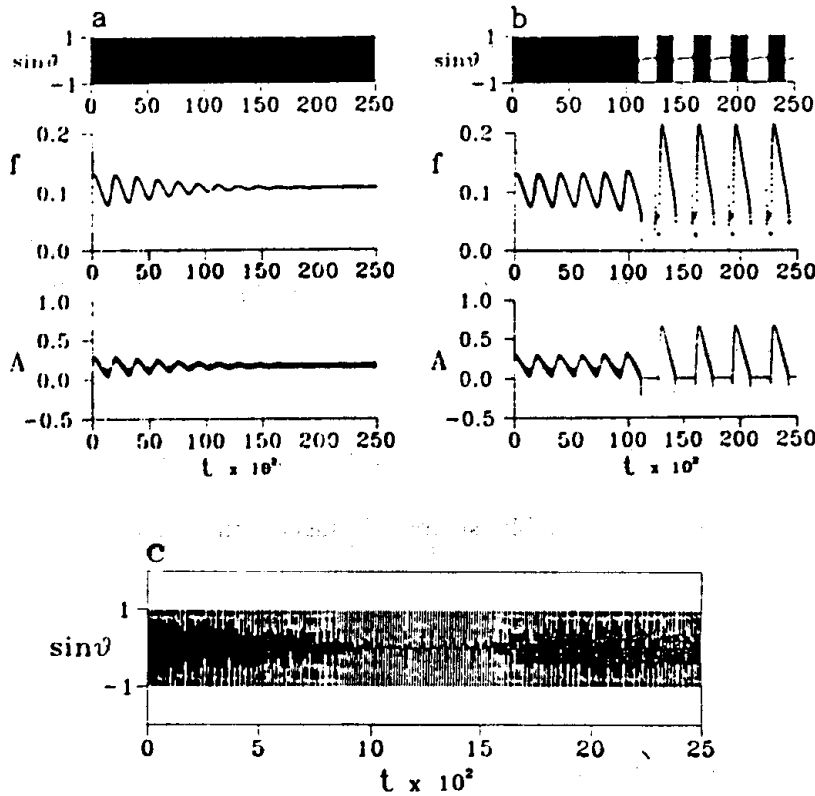


Fig. 11. Bistable behavior of  $\varepsilon_x \ll \varepsilon_y$ . Same parameters as in Fig. 9, but all solutions are computed directly from the full model (1)–(3). Using the reduced system's bifurcation diagram as a guide,  $I$  is fixed at 0.24, in the vicinity of bistability. Slow variables are set initially to  $x_0 = 0.4980884$  and  $y_0 = 0.2013005$  corresponding to stable continuous spiking. **a** *Top*: in response to a small amplitude perturbation from stable continuous spiking ( $x_0$  perturbed by  $\delta = 0.18000 \times 10^{-2}$ ), the full system returns to continuous spiking through frequency modulated spiking, although on this time scale frequency modulations cannot be resolved (see (c) below). *Middle*: the frequency of fast oscillations plotted as a function of time decays to steady-state. *Lower*: the related activation function also decays to steady-state. **b** In response to a larger perturbation ( $\delta = 1.9173 \times 10^{-2}$ ), modulated spiking grows (middle and lower) until the onset of bursting, which occurs at about  $t = 110 \times 10^2$ . The top graph shows the onset of bursting, but as in (a) frequency modulations cannot be resolved on this time scale. **c** Unstable modulated spiking: expanded view of the top time course in (a) for  $t$  between 0 and 2500. On this scale frequency modulation can be observed

predicted from the bifurcation diagram of the reduced subsystem in Fig. 9: label b is closer to the homoclinic point of bifurcation than label c. This explains why during the silent phase the time course (inset) appears flat. This feature, common to all panels of Fig. 10, is not usually associated with parabolic burst activity: typically, trajectories characteristically ride on sinusoidal-like slow waves.

Figure 10d illustrates continuous spiking. Observe the indirect path followed by a trajectory initiated in the silent region. The trajectory first drops

sharply to  $A = 0$ , hugs this line until it reaches the cusp, then crosses into the active region where it finally approaches the fixed point. Thus, common to both Figs. 7 and 10, large net stimuli result in continuous spiking, which is consistent with the bifurcation structure and our intuition.

## 5 Discussion

We have formulated a minimal phase model for endogenous parabolic bursting. The model is analyzed by deriving a reduced set of equations for the slow variables, using quasi steady-state assumptions and formal averaging (over fast spiking). This reduced system is used to estimate parameter values where the full model exhibits bursting, steady-states, continuous and modulated spiking. We find conditions for the bistability of solutions between continuous spiking and bursting, and find that the relative speed of activation ( $\epsilon_x$ ) and inactivation ( $\epsilon_y$ ) of the slow variables strongly influences the burst pattern as well as other dynamics.

When the speed of inactivation is slower than activation burst solutions ride on underlying slow oscillations, characteristic of a bursting pacemaker neuron such as the R-15 cell of *Aplysia*. The slow wave emerges without spikes for parameter values which destabilize (Hopf) the resting state in the silent region. When activation is slower there is no slow wave (compare Fig. 7c with Fig. 10b or c). Furthermore, the bifurcation structures are different (cp., Figs. 8 and 9). When  $\epsilon_y \ll \epsilon_x$ , complicated solutions, possibly chaotic, can exist over a wide range of parameter values. Our numerical studies indicate that burst solutions become less organized and irregular as the cusp is approached. Terman [31] has addressed some of these questions using geometric singular perturbation theory, but for a different model. When  $\epsilon_x \ll \epsilon_y$ , the parameter range for unusual burst solutions is small, but the possibility of modulated continuous spiking arises and bistability occurs in the vicinity of the Hopf point where the steady CS solution destabilizes.

Our slow phase plane analysis reveals the geometrical features that underlie the emergence via Hopf bifurcation of slow wave and modulated continuous spiking solutions. In the first case, onset of PSW (Fig. 7b and Fig. 8), the activation nullcline ( $y$  vs.  $x$ ) in the silent region is non-monotonic. This behavior sets up the possibility for Hopf bifurcation when activation is fast and the steady state moves by parameter across the nullcline's minimum. In the second case, the inactivation nullcline ( $x$  vs.  $y$ ) in the active region is non-monotonic. Correspondingly, when inactivation is fast, a steady state just inside the  $y$ -nullcline minimum can change stability via Hopf bifurcation as parameters are varied. These are instances of a general property in two-variable relaxation systems (think of FitzHugh-Nagumo as an example) with the fast variable having a cubic-like nullcline: Hopf bifurcation and onset of oscillations occurs when a steady state moves onto or off of the fast variable nullcline's middle branch. The non-monotone features depend on parameter values in our model, and for some cases (not shown here) these features are not present.

The phase burster exhibits dynamics remarkably similar to more complex models of parabolic bursting. We do not expect the dynamics to be identical for two reasons: first, we have simplified the fast system using a simple phase representation and second, the slow equations can vary from model to model. The phase burster's slow equations also have a very simple form.

The phase model may be viewed as a canonical description of more complex models, in much the same way the FitzHugh-Nagumo [11] equations serve in studying features of the Hodgkin-Huxley system. To demonstrate this, consider Rinzel and Lee's model for a parabolic burst mechanism based on calcium-inactivation of a calcium conductance, which they call the Ca-Ca model [26]. The equations for the fast dynamics of the Ca-Ca model have a Hodgkin-Huxley like form:

$$C_m \dot{V} = -\bar{g}_{Na} m_x^3(V) h(V - V_{Na}) - \bar{g}_K n^4(V - V_K) - \bar{g}_L(V - V_L) \\ - \bar{g}_{Ca-Ca} X H(Ca)(V - V_{Ca}) - \bar{g}_{K.o}(V - V_K) \quad (33)$$

$$\dot{h} = \lambda(h_\infty - h)/\tau_h \quad (34)$$

$$\dot{n} = \lambda(n_\infty - n)/\tau_n \quad (35)$$

Here,  $V$  denotes membrane potential ( $mV$ );  $h$  is a  $V$ -dependent, HH-like inactivation variable for Na-channels, and  $n$  is the activation of HH K-Channels.  $H(Ca)$  is a nonlinear inactivation function which responds instantaneously to  $Ca$ . The slow dynamics is governed by

$$\dot{X} = [X_\infty(V) - X]/\tau_X \quad (36)$$

$$\dot{Ca} = \rho[Ca_\infty(V, X, Ca) - Ca] \quad (37)$$

where  $X$  is an activation variable which controls the inward calcium conductance represented as  $\bar{g}_{Ca-Ca} X H(Ca)$ , and  $Ca$  is the slowly changing concentration of cytoplasmic free calcium which acts to depress or inactivate the fast spike generating system (33)–(35). In comparison to the phase burster model (1)–(3),  $X$  is analogous to  $x$  and  $Ca$  is analogous to  $y$ ; with the important difference that  $Ca_\infty$  is a function of the two slow variables in addition to a fast variable, whereas  $y_\infty$  is a function of the fast variable  $\theta$  only. The parameters and nonlinear functions for (33)–(37) are listed in the Appendix. A more detailed description of the Ca-Ca model can be found in Rinzel and Lee [26]. Canavier et al. [5] have also formulated a biophysical Ca-Ca model.

In Fig. 12a burst solution to (33)–(37) is projected into the plane  $Ca - X$  of slow variables. We have labelled the axes in reverse with inactivation horizontal and activation vertical; the reason is so that Fig. 12 can be compared directly to Rinzel and Lee's Fig. 8 (which is computed with the same parameter values as our Fig. 12). New in our figure is the inclusion of the averaged  $X$  and  $Ca$ -nullclines. We computed these nullclines using the numerical procedure described recently by Smolen et al. [29], which uses the bifurcation code AUTO to find nullclines for the slow variables when the fast variables are periodic, by averaging over the fast oscillations. This procedure is time consuming and of course not necessary for the phase burster, since averaged equations are derived in closed form.

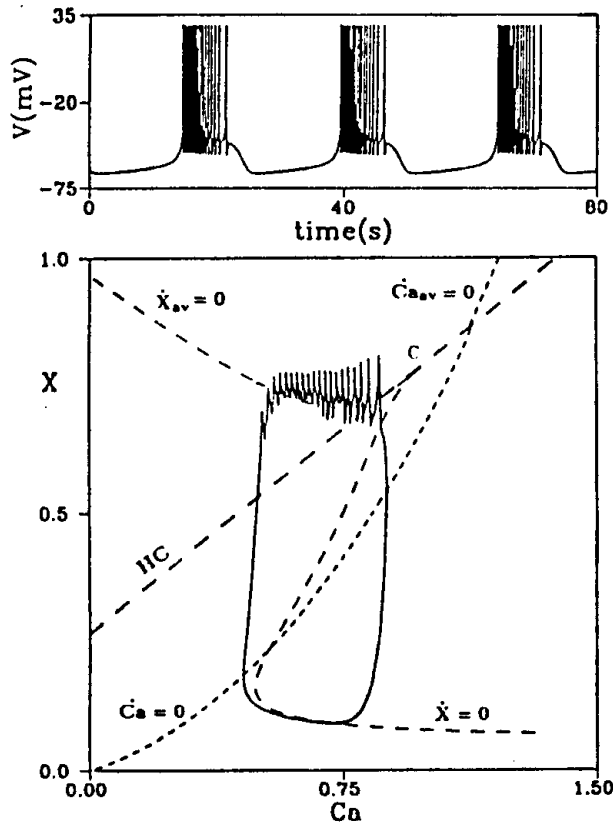


Fig. 12. Burst solution of Rinzel and Lee's Ca-Ca model [26] follows the  $X_{av}$ -nullcline in the active phase. Projection of solutions to (33)–(37) onto plane  $Ca - X$  of slow variables. Curve HC corresponds to degenerate homoclinic orbit. As in Fig. 8 of [26],  $\rho = 10^{-4}$  and  $\tau_x = 235$ . Other parameter values are given in the Appendix. The nullclines from the active and silent regions meet to form a cusp at C

A prominent feature in Fig. 12 is the cusp formed where the  $X$ -nullcline from the silent region and its averaged counterpart meet along HC. The  $Ca$ -nullcline also has a cusp on HC, but is small and difficult to see in Fig. 12. Our phase plane analysis of the phase burster model suggested that such cusp-like structure should occur in the Ca-Ca model.

Finally, we can deduce that the bifurcation structure of the Ca-Ca model is qualitatively similar to the supercritical structure in Fig. 8; i.e., stable steady states give rise to slow oscillations followed by bursting and continuous spiking as  $1/K_c$  increases. The parameter  $K_c$  controls the  $Ca$ -nullcline, and as Rinzel and Lee point out, increasing  $K_c$  rotates the nullcline clockwise. Therefore, increasing  $1/K_c$  drives the equilibrium point up through the cusp and over onto the oscillatory side, where the equilibrium point becomes stable; this is the continuous spiking case. The reciprocal of  $K_c$  is proportional to the removal rate of calcium; a low removal rate corresponds to a stable steady state, a high rate continuous spiking. In this sense  $1/K_c$  is analogous to our net stimulus parameter  $I$ . In Fig. 12,  $\rho < 1/\tau_x$ , which is consistent with inactivation ( $\tau_y$ ) being slower than activation ( $\tau_x$ ) in the phase model.

## Appendix: parameters and functions for the Ca-Ca model

For  $\dot{V}$ :

$$\begin{aligned}
 C_m &= 1 \mu\text{F}/\text{cm}^2 \\
 V_{Na} &= 30 \text{ mV}, \quad V_{Ca} = 140 \text{ mV}, \quad V_K = -75 \text{ mV}, \quad V_L = -40 \text{ mV}, \\
 \bar{g}_{Na} &= 4.0 \text{ mS}/\text{cm}^2, \quad \bar{g}_K = 0.3 \text{ mS}/\text{cm}^2, \quad \bar{g}_L = 0.003 \text{ mS}/\text{cm}^2 \\
 \bar{g}_{Ca-Ca} &= 0.009 \text{ mS}/\text{cm}^2, \quad \bar{g}_{K,0} = 0.015 \text{ mS}/\text{cm}^2 \\
 m_x(V) &= \frac{x_m(\tilde{V})}{x_m(\tilde{V}) + \beta_m(\tilde{V})}, \quad \tilde{V} = \frac{127}{105} V + \frac{8265}{105},
 \end{aligned}$$

where

$$x_m(V) = \frac{0.1(50 - V)}{e^{(50 - V)/10} - 1}, \quad \beta_m(V) = 4e^{(25 - V)/18},$$

For  $\dot{h}$ :

$$h_x(V) = \frac{x_h(\tilde{V})}{x_h(\tilde{V}) + \beta_h(\tilde{V})}, \quad \tau_h(V) = \frac{1}{x_h(\tilde{V}) + \beta_h(\tilde{V})}, \quad \lambda = 1/12.5,$$

where

$$x_h(V) = 0.07e^{(25 - V)/20}, \quad \beta_h(V) = \frac{1}{e^{(55 - V)/10} + 1}.$$

For  $\dot{n}$ :

$$n_x(V) = \frac{x_n(\tilde{V})}{x_n(\tilde{V}) + \beta_n(\tilde{V})}, \quad \tau_n(V) = \frac{1}{x_n(\tilde{V}) + \beta_n(\tilde{V})},$$

where

$$x_n(V) = \frac{0.01(55 - V)}{e^{(55 - V)/10} - 1}, \quad \beta_n(V) = 0.125e^{(45 - V)/80}.$$

For  $\dot{X}$  and  $\dot{Ca}$ :

$$X_x(V) = \frac{1}{e^{-0.15(50 + V)} + 1},$$

$$Ca_x(V, X, Ca) = K_C X H(Ca)(V_{Ca} - V),$$

$$H(Ca) = \frac{1}{1 + 2Ca},$$

where

$$K_C = 2.343 \times 10^{-2} \text{ mV}^{-1},$$

$$\rho = 10^{-4} \text{ ms}^{-1} \quad \text{and} \quad \tau_X = 235 \text{ ms}$$

## References

1. Ashcroft, F., Rorsman, P.: Electrophysiology of the pancreatic  $\beta$ -cell. Prog. Biophys. Molec. Biol. **54**, 87-143 (1989)
2. Baer, S. M., Erneux, T.: Singular Hopf bifurcation to relaxation oscillations. SIAM J. Appl. Math. **46**, 721-739 (1986)

3. Baer, S. M., Erneux, T.: Singular Hopf bifurcation to relaxation oscillations II. *SIAM J. Appl. Math.* **52**, 1651–1664 (1992)
4. Canavier, C. C., Baxter, D. A., Clark, J. W., Byrne, J. H.: Nonlinear dynamics in a model neuron provide a novel mechanism for transient synaptic inputs to produce long term alterations of postsynaptic activity. *J. Neurophysiol.* **69**, 2252–2257 (1993)
5. Canavier, C. C., Clark, J. W., Byrne, J. H.: Simulation of the bursting activity on neuron R15 in *Aplysia*: role of ionic currents, calcium balance, and modulatory transmitters. *J. Neurophysiol.* **66**, 2107–2124 (1991)
6. Doedel, E.: AUTO: A program for the automatic bifurcation analysis of autonomous systems. *Cong. Num.* **30**, 265–284 (1981)
7. Ermentrout, G. B.: *EPHASEPLANE: The dynamical systems tool*, Version 3.0. Brooks/Cole Publishing Co. Pacific Grove, CAL 1990
8. Ermentrout, G. B., Kopell, N.: Parabolic bursting in an excitable system coupled with a slow oscillation. *SIAM J. Appl. Math.* **46**, 233–253 (1986)
9. Ermentrout, G. B., Rinzel, J.: Waves in a simple, excitable or oscillatory reaction-diffusion model. *J. Math. Biol.* **11**, 269–294 (1981)
10. Ermentrout, G. B.: Reduction of conductance-based models with slow synapses to neural nets. *Neur. Comput.* (in press)
11. FitzHugh, R.: Mathematical models for excitation and propagation in nerve. In: Schwan, H.P. (ed.) *Biological Engineering*. New York: McGraw Hill 1969
12. Gear, C.: The numerical integration of ordinary differential equations. *Math. Comp.* **21**, 146–156 (1967)
13. Gerald, C. F.: *Applied Numerical Analysis*. Reading, MA: Addison-Wesley 1978
14. Grasman, J.: *Asymptotic Methods for Relaxation Oscillations and Applications*. Applied Mathematical Sciences **63**. Berlin Heidelberg New York: Springer: 1987
15. Guckenheimer, J., Holmes, P.: *Nonlinear Oscillations, Dynamical Systems, and Bifurcations of Vector Fields*. Applied Mathematical Sciences **42**. Berlin Heidelberg New York: Springer: 1983
16. Hille, B.: *Ionic Channels of Excitable Membranes* (2nd ed.). Sunderland, MA: Sinauer Associates 1992
17. Hodgkin, A., Huxley, A.: A quantitative description of membrane current and its application to conduction and excitation in nerve. *J. Physiol. (Lond.)* **117**, 500–544 (1952)
18. Hoppensteadt, F.: Singular perturbations on the infinite interval. *Trans. Amer. Math. Soc.* **123**, 521–535 (1966)
19. Keizer, J.: Electrical activity and insulin release in pancreatic  $\beta$ -cells. *Math. Biosci.* **90**, 127–138 (1988)
20. Kevorkian, J., Cole, J. D.: *Perturbation Methods in Applied Mathematics*. Applied Mathematical Sciences **34**. Berlin Heidelberg, New York: Springer 1981
21. Morris, C., Lecar, H.: Voltage oscillations in the barnacle giant muscle fiber. *Biohys. J.* **35**, 193–213 (1981)
22. Pernarowski, M., Miura, R. M., Kevorkian, J.: Perturbation techniques for models of bursting electrical activity in pancreatic  $\beta$ -cells. *SIAM J. Appl. Math.* **52**, 1627–1650
23. Plant, R. E.: Bifurcation and resonance in a model for bursting nerve cells. *J. Math. Biol.* **11**, 15–22 (1981)
24. Rinzel, J., Ermentrout, G. B.: Analysis of neural excitability and oscillations. In: Koch, C., Segev, I. (eds.) *Methods in neuronal modeling: from synapses to networks* pp. 135–169. Cambridge: MIT Press 1989
25. Rinzel, J., Frankel, P.: Activity patterns of a slow synapse network predicted by explicitly averaging spike dynamics. *Neur. Comput.* **4**, 534–545 (1992)
26. Rinzel, J., Lee, Y. S.: Dissection of a model for neuronal parabolic bursting. *J. Math. Biol.* **25**, 653–675 (1987)
27. Rinzel, J.: A formal classification of bursting mechanisms in excitable systems. In: Teramoto E., Yamaguti, M. (eds.) *Mathematical topics in population biology, morphogenesis, and neurosciences Lect. Notes Biomath., Vol. 71*. Berlin, Heidelberg, New York: Springer 1987
28. Sanders, J. A., Verhulst, F.: *Averaging methods in nonlinear dynamical systems*. Berlin Heidelberg New York: Springer 1985



29. Smolen, P., Terman, D., Rinzel, J.: Properties of a bursting model with two slow inhibitory variables. *SIAM J. Appl. Math.* **53**, 861–892 (1993)
30. Mirollo, R. E., Strogatz, S. H.: Synchronization of pulse-coupled biological oscillators. *SIAM J. Appl. Math.* **50**, 1645–1662 (1990)
31. Terman, D.: Chaotic spikes arising from a model for bursting in excitable membranes. *SIAM J. Appl. Math.* **51**, 1418–1450 (1991)
32. Tikhonov, A. N.: Systems of differential equations containing a small parameter multiplying the highest derivatives. *Mat. Sb. Ns.* (31) **73**, 575–585 (1952)
33. Winfree, A. T.: *The geometry of biological time*. Heidelberg Berlin New York: Springer 1980